

Ensemble Mapping the Inner Structure of Luminous Quasars

Liang Wu^{1,2}★ Jun-Xian Wang^{1,2}† Hao-Chen Wang^{1,2} Wen-Yong Kang^{1,2} Wei-Da Hu^{1,2}
Ting-Gui Wang^{1,2} and Hui-Yuan Wang^{1,2}

¹CAS Key Laboratory for Research in Galaxies and Cosmology, Department of Astronomy, University of Science and Technology of China, Hefei, Anhui 230026, China

²School of Astronomy and Space Science, University of Science and Technology of China, Hefei 230026, China

Accepted XXX. Received YYY; in original form ZZZ

ABSTRACT

A simple prediction of the well-known unification model of active galactic nuclei is that a sample of sources should exhibit an anti-correlation between the solid angle of the dusty torus and of the ionization cone (as the sum of them shall equal 4π), which however has never been detected. In this work, we analyze the correlation between [OIII] 5007 narrow emission line equivalent width and $L_{\text{IR}}(\lambda)/L_{\text{bol}}$ for a large sample of luminous quasars. For the first time, we detect a clear intrinsic anti-correlation between them, which immediately verifies the torus/ionization-cone geometry in luminous quasars. More interestingly, the anti-correlation significantly weakens with increasing wavelength from ~ 2 to $12 \mu\text{m}$, and disappears at $\sim 12 \mu\text{m}$. Simulations show a cool dust component (in addition to equatorial torus) with its strength positively correlating with the solid angle of the ionization cone is required to explain the observations. This shows that the polar dust seen in nearby active galaxies also exists in luminous quasars, with its contribution to total dust emission increasing with λ (from ~ 2 to $12 \mu\text{m}$) and reaching between 39%–62% (model dependent) at rest frame $12 \mu\text{m}$. Our findings provide a unique approach to map the otherwise spatially unresolvable inner structure of quasars.

Key words: galaxies: active — quasars: general

1 INTRODUCTION

The key gradient in the renowned unification scheme of active galactic nuclei is the dusty toroidal structure in the equatorial plane, namely the torus (e.g. Antonucci 1993; Urry & Padovani 1995). The torus obscures radiation from the central engine (re-emits in infrared), and results in the bi-polar ionization cones where narrow emission lines are produced (i.e, the narrow line region, NLR) as detected in many local AGNs and quasars (Evans et al. 1991; Müller-Sánchez et al. 2011; Storchi-Bergmann et al. 2018). The torus is widely believed to be clumpy (e.g. Krolik & Begelman 1988; Nenkova et al. 2008), with the innermost part (named hot dust, Barvainis 1987) emitting at sublimation temperature $T \sim 500 - 2000\text{K}$, and outer part with lower temperature. However, while the equatorial dusty structure has been resolved in some nearby active galaxies (e.g. Jaffe et al. 1996; Leftley et al. 2021), they are far from resolvable in most quasars which are far more distant.

Apart from the toroidal torus, recent high-resolution mid-infrared observations have revealed polar elongated dust emission ubiquitously in nearby AGNs, on scales up to tens or larger parsecs (e.g. Asmus et al. 2016; López-Gonzaga et al. 2016; Asmus 2019)¹. Such polar dust, tentatively associated with dusty winds (Hönig & Kishi-

moto 2017; Stalevski et al. 2019), or the dusty NLR (e.g. Netzer & Laor 1993; Schweitzer et al. 2008; Mor et al. 2009; Mor & Netzer 2012; Asmus et al. 2016), is expected to be cooler than the hot dust at smaller scales, and could dominate the mid-infrared emission in AGNs.

Within the unification scheme, one can easily foresee a consequence, which however has never been detected, that a sample of sources should exhibit an anti-correlation between the solid angle of the torus and of the ionization cone, i.e., sources with larger solid angle of the torus shall have smaller solid angle of the ionization cone (as the sum of them shall equal 4π). The ratio of monochromatic or integrated infrared luminosity to bolometric luminosity has widely been adopted to quantify the covering factor of the dusty torus in AGNs (e.g. Maiolino et al. 2007; Roseboom et al. 2013; Ma & Wang 2013; Wang et al. 2013; Netzer 2015; Stalevski et al. 2016). This approach is further supported by the fact that for clumpy torus, the IR SEDs barely change with viewing angle, as long as for type 1 AGNs (viewed along dust-free line of sight, Stalevski et al. 2012)².

While there are many factors which could affect the observed $L_{\text{IR}}/L_{\text{bol}}$ in AGNs (see discussion in §4), clearly, for individual sources in a large sample of AGNs, the ratio of torus IR emission to bolometric luminosity is expected to positively correlate with the solid angle of the torus. Contrarily, the opposite would be true for

★ E-mail: wul@mail.ustc.edu.cn

† E-mail: jxw@ustc.edu.cn

¹ Alternatively, Nikutta et al. (2021) proposed that, under specific conditions, clumpy equatorial tori could exhibit morphologies with significant polar elongation in the mid-infrared.

² However note recent works suggested that the connection between $L_{\text{IR}}/L_{\text{bol}}$ and torus covering factor is likely non-linear (Stalevski et al. 2016; Toba et al. 2021) because of the possible anisotropic radiation from the accretion disk. Such effect would be discussed in §4.2.

the polar dust, whose radiation is expected to correlate with the solid angle of the ionization cone. Meanwhile, [OIII] 5007 is the most prominent narrow emission line in the optical spectra of quasars and AGNs, with its luminosity expected to be proportional to the covering factor of the narrow line region, therefore, of the ionization cone.

In this work for simplicity we define $CF(\lambda)$ as the ratio of monochromatic infrared luminosity at wavelength λ to bolometric luminosity. We aim to explore the correlation between $L_{IR}(\lambda)/L_{bol}$ and O[III] EW, two quantities served as proxies of the solid angles of the dusty structure and the ionization cone respectively, of a large sample of luminous quasars. We expect to detect negative correlation between two quantities if the observed $L_{IR}(\lambda)$ is torus dominated, and contrarily negative correlation if polar dust dominated. By exploring such correlation and its dependence on λ , we could uniquely and ensemble map the otherwise spatially unresolvable inner structure of quasars. The paper is organized as follows: In §2, we illustrate the sample selection and the measurements of $L_{IR}(\lambda)/L_{bol}$. In §3, we describe the correlation analyses and show the results. We discuss the results in §4 and summarize in §5.

2 THE SAMPLE AND THE MEASUREMENTS OF

$L_{IR}(\lambda)/L_{BOL}$

2.1 The Sample

We start from the Sloan Digital Sky Survey (Eisenstein et al. 2011) data release 7 quasar catalogue (Schneider et al. 2010). The multi-band photometry, including SDSS (Fukugita et al. 1996), 2MASS³ (Carpenter 2001) and WISE (Wright et al. 2010), and SDSS spectral fitting results (line EW, and supermassive black hole mass) were taken from Shen et al. (2011). We exclude quasars with redshift $z > 0.797$ to ensure the coverage of [OIII] 5007 emission line in SDSS spectra. To avoid contamination from the host galaxy, following (Roseboom et al. 2013) we focus on the 1953 luminous quasars with bolometric luminosity from Shen et al. (2011)⁴ above 10^{46} erg/s. We select 1891 sources with 2MASS and WISE detections and the signal to noise ratio (S/N) in all WISE bands greater than 3. Note that since we focus on luminous quasars, utilizing the latest data release (DR16) of SDSS quasar catalog (Lyke et al. 2020) could only increase the sample size by $\sim 20\%$. 238 sources (12.6%) in our sample have radio loudness $R = F_{\nu,6cm}/F_{\nu,2500\text{\AA}}$ greater than 10, which can be regarded as radio loud (Kellermann et al. 1989). Excluding them from this study would not significantly alter the results presented in this work.

2.2 Measuring $L_{IR}(\lambda)/L_{bol}$

In literature, the dust emission $L_{IR}(\lambda)$ is commonly derived through SED-fitting the broadband (UV/optical to infrared) photometric data, adopting various templates of disc and dust emission, such as the popular hot+cold dust model (e.g. Roseboom et al. 2013), and X-Cigale (Yang et al. 2020). Clearly, as the broadband SED is sparsely sampled in wavelength, these physical models would yield significantly

model/template dependent measurements, and properly decomposing the various dust components thus would be highly challenging. In this work we aim to perform ensemble analyses without the need to decomposing the dust components in individual sources (thus without prior assumptions of the dust templates, which is one unique feature of this work). To do so, we simply interpolate the SED to measure $L_{IR}(\lambda)$ in a template-independent manner.

Before that, we first show the SED-fitting with the hot+cold dust model of Roseboom et al. (2013), the measurements of accretion disc component of which could be used in this work. In the model, the template of the accretion disk component consists of two parts connected at $0.7 \mu\text{m}$: the $0.05 - 0.7 \mu\text{m}$ radio quiet quasar template from Shang et al. (2011) and a power-law of $\lambda L_{\lambda} \propto \lambda^{-1}$ at $\lambda > 0.7 \mu\text{m}$. Hot dust refers to the dust at or close the sublimation radius which mainly radiate in near-IR and is modeled with a single black body (with temperature ranging from 500 K to 2000 K). The 3rd component is to describe the colder dust emission (presumably in the dusty torus, but see later for discussion). Three cold dust templates from Nenkova et al. (2008) are adopted (see table 2 in Roseboom et al. 2013, for model parameters), and the one which yields the least χ^2 among the three is selected for an individual quasar. Extinction with a SMC-like extinction curve (Gordon et al. 2003) is considered. Negative extinction is allowed during the fitting to handle a significant fraction of optical/UV SEDs which are bluer than the disc template (as the disc template itself could have been slightly reddened). Contributions of the host galaxies are not considered. We plot in Fig. 1 an example fit to an individual quasar. For most sources, the model we adopted yields reasonably good fits. The yielded χ^2 (reduced χ^2) has a median value of 28.9 and a mean of 43.1 for a degree of freedom of 7.⁵ However, there are still a small amount of sources that are poorly fitted. One possible reason is strong extinction, which may not be well fitted with a simple SMC extinction curve. Strong extinction can also affect the measurements of other SED parameters. Thus we drop sources with $\chi^2 > 50$ or $A_V > 0.5$ from following studies in this work, although keeping them would not alter the main results presented in this work. Eventually, 1459 sources are left. For each source we derive L_{bol} from the monochromatic luminosity of disk template at 5100\AA adopting a constant bolometric correction factor of 9.26 (the same as that utilized in Shen et al. 2011). We also calculate the total dust emission through integrating the best-fit model within $1 - 10 \mu\text{m}$, and derive the corresponding $L_{IR}^{dust}(1 - 10\mu\text{m})/L_{bol}$ (hereafter CF0). We plot in Fig. 2 the SED fitting residuals for all sources. While the hot+cold dust model yields reasonable fit to UV/optical, clear systematical residuals are seen in infrared.

We then perform cubic spline interpolation to fit the SED (see Fig. 1 and 2), which well describe the data and yield no clear systematical residuals. The best-fit SED shape derived through cubic spline interpolation however appears significantly different from that of the hot+cold dust model at longest wavelengths (see Fig. 1). To further examine whether the results in this work is sensitive to the selected interpolation function, we also perform linear interpolation (the most simple form of interpolation).

Hereafter we proceed with $L_{IR}(\lambda)$ measured using cubic spline and linear interpolation, which are simple and template independent. Since the hot+cold dust model yields reasonable fit to UV/optical

³ UKIDSS (Lawrence et al. 2007) is the successor to 2MASS, with one more band (Y band), and better data quality. However, it currently only covers 4000 deg^2 of the sky and only 217 sources (11.5%) in our sample can be found in the catalog of UKIDSS.

⁴ The bolometric luminosity provided by Shen et al. (2011) was converted from L_{5100} (measured from SDSS spectral fitting) with a constant bolometric correction factor of 9.26.

⁵ The median and mean χ^2 we derived are about 2 times larger than those reported by Roseboom et al. (2013), the reason of which is yet unclear. In fact, if fitting the same SED data points of Roseboom et al. (2013), i.e., SDSS + UKIDSS + WISE, instead of SDSS + 2MASS + WISE adopted in this work, we obtain even larger χ^2 . It is likely that Roseboom et al. (2013) has added extra photometric errors to SED data points.

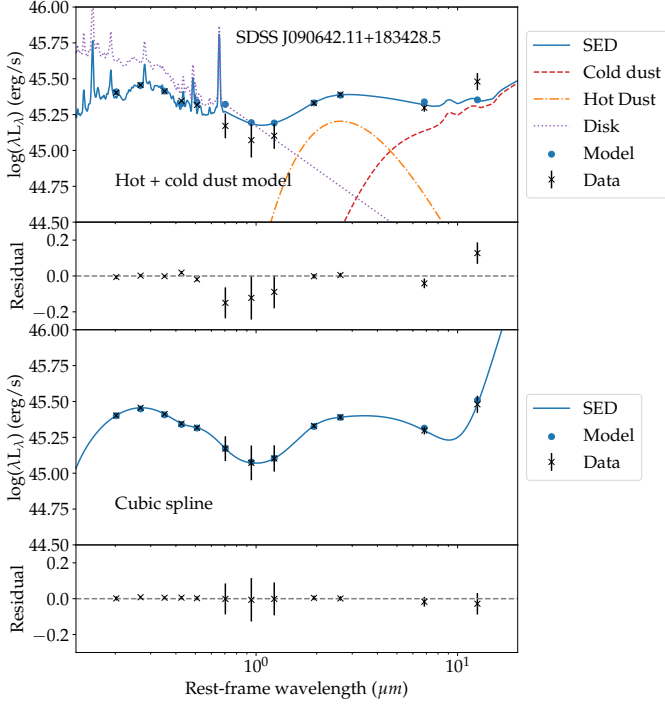


Figure 1. Example SED fitting of a randomly chosen source SDSS J090642.11+183428.5, using the hot+cold dust model (upper), and the cubic spline fit (lower). Note as the model luminosity in a given band is calculated by convolving the model spectrum over the response curve of each band, the model SED data points do not necessarily fall right on the model spectra.

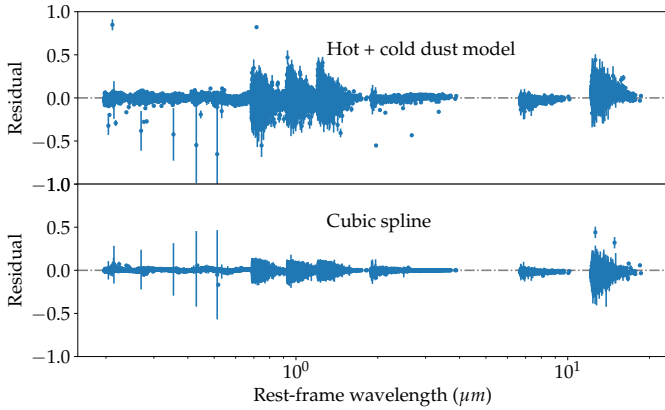


Figure 2. Residuals from all bands of all sources of hot+cold dust model (upper), and cubic spline fit (lower).

data (see the upper panel in Fig. 2), we directly take its output L_{bol} (converted from L_{5100} of the best-fit disc template) to calculate $L_{\text{IR}}(\lambda)/L_{\text{bol}}$. We further note that, if we assume a AGN disc component with a given template (as adopted in the hot+cold dust model), $L_{\text{IR}}(\lambda) = k_{\lambda}L_{\text{bol}} + L_{\lambda}^{\text{dust}}$, where k at given infrared wavelength is simply a constant for different sources. Therefore we do not need to subtract the disc component from the interpolated $L_{\text{IR}}(\lambda)$, as it does not affect the correlation analyses presented below.

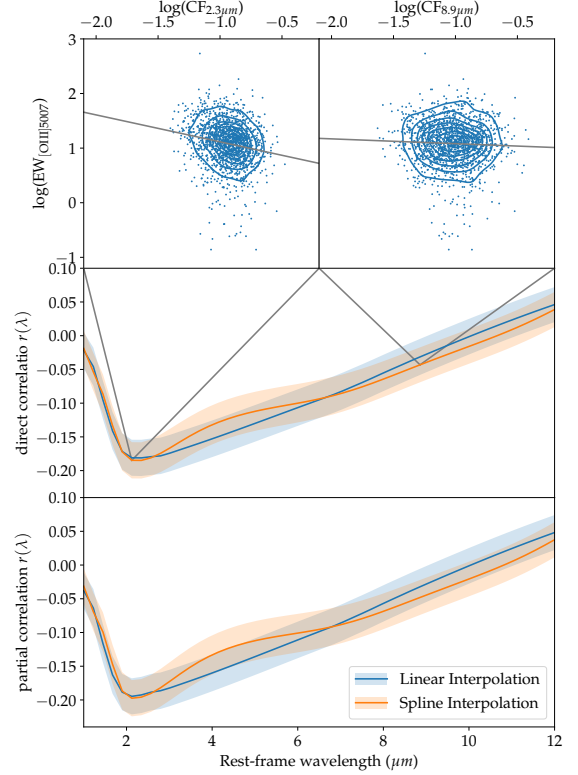


Figure 3. Direct (middle panel) and partial correlation (lower panel) coefficient r between $\text{EW}_{[\text{OIII}]5007}$ and $\text{CF}(\lambda)$ as a function of λ over rest-frame 1–12 μm . Shadows plot the 1σ confidence errors derived through bootstrapping the sample. To directly demonstrate the correlations, in the upper panels we plot $\text{EW}_{[\text{OIII}]5007}$ versus $\text{CF}(\lambda)$ (calculated with spline interpolation for example) and the best-fit linear regression at 2.3 and 8.9 μm , respectively.

3 CORRELATION ANALYSES

We perform Pearson correlation between $\text{EW}_{[\text{OIII}]5007}$ and $\text{CF}(\lambda)$ of our sample and present the resulted correlation coefficient $r(\lambda)$ in Fig. 3. We estimate the uncertainties in $r(\lambda)$, which are also useful to demonstrate the statistical significance of the correlation, through bootstrapping the quasar sample. The upper wavelength bound of $r(\lambda)$ is set at 12 μm , corresponding to the rest frame wavelength that WISE W4 (22.19 μm) could probe for the highest redshift quasars ($z=0.797$) in the sample.

Before we interpret the derived $r(\lambda)$, we note that both $\text{EW}_{[\text{OIII}]5007}$ and $\text{CF}(\lambda)$ may correlate with fundamental parameters of quasars, including bolometric luminosity L_{bol} , supermassive black hole mass M_{BH} (and also the Eddington ratio), and such correlations may produce artificial direct correlation between $\text{EW}_{[\text{OIII}]5007}$ and $\text{CF}(\lambda)$.

Note for each source we have two L_{5100} (and $L_{\text{bol}} = 9.26 * L_{5100}$), one obtained through SDSS spectral fitting (Shen et al. 2011), and another from SED fitting to photometric data (§2.2). Two L_{5100} could be different due to the intrinsic variability since the SDSS photometric and spectroscopic observations were not taken simultaneously. Hereafter we adopt the SED-fitting based L_{5100} and L_{bol} , though

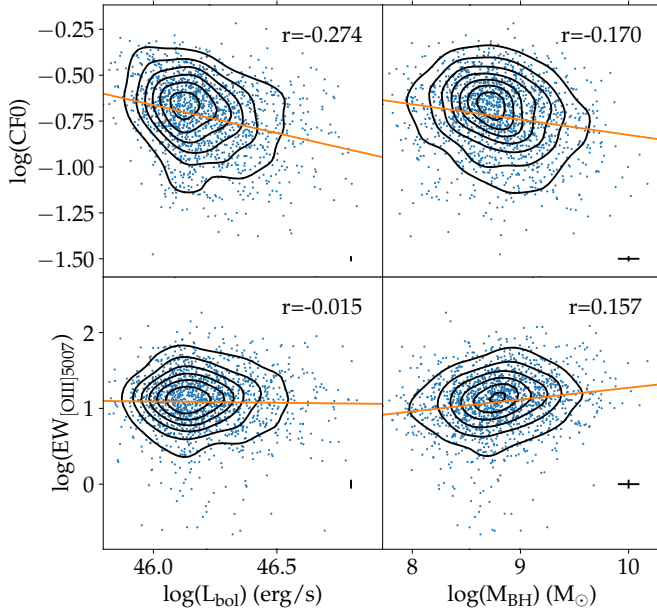


Figure 4. $\text{EW}_{[\text{OIII}]5007}$ and CF_0 versus bolometric luminosity L_{bol} and black hole mass M_{BH} , respectively. Simple linear regressions are performed and shown as solid lines. The error bars in the lower right corner of each panel mark the median 1σ errors of the corresponding parameters for the sample. The uncertainties in M_{BH} and $\text{EW}_{[\text{OIII}]5007}$ are from Shen et al. (2011), and those for CF_0 and L_{bol} are from SED fitting obtained through adding random Gaussian photometric errors to SED data points. Clearly the statistical errors of the parameters are small comparing with the scatter in the plot, and are ignored in correlation analyses (hereafter the same). The correlation coefficients r between the quantities are labelled.

simply utilizing L_{bol} from Shen et al. (2011) would not alter the key results presented in this work.

In Fig. 4 we draw scatter plots presenting the dependence of $\text{EW}_{[\text{OIII}]5007}$ and CF_0 (see §2.2 for definition) on L_{bol} and M_{BH} , respectively. We see clear anti-correlations between CF_0 and both L_{bol} and M_{BH} , consistent with previous studies (e.g. Ma & Wang 2013; Mor & Trakhtenbrot 2011; Calderone et al. 2012). EW appears positively correlate with M_{BH} , but we find no apparent correlation between $\text{EW}_{[\text{OIII}]5007}$ and L_{bol} . This seems against the well known Baldwin effect (e.g. Baldwin 1977; Baldwin et al. 1978; Croom et al. 2002; Netzer et al. 2004; Kovačević et al. 2010; Zhang et al. 2011, 2013). This is because 1) the $L_{\text{bol}} (= 9.26 * L_{5100})$ adopted in Fig. 4 was obtained through fitting the photometric data points, independent to SDSS spectra where $[\text{OIII}] 5007$ EWs were measured, 2) no intrinsic extinction correction was applied to the spectroscopic L_{5100} from Shen et al. (2011), and 3) our sample only contains the most luminous sources spanning a rather narrow luminosity range. Simply adopting the spectroscopic L_{5100} from Shen et al. (2011) for the whole SDSS DR7 catalog, we do see clear Baldwin effect of $[\text{OIII}] 5007$, with $\text{EW} \sim L_{5100}^{-0.21 \pm 0.009}$ ($r = -0.183$), consistent with the results reported in literature (e.g. Croom et al. 2002; Kovačević et al. 2010; Zhang et al. 2013). Replacing the spectroscopic L_{5100} from Shen et al. (2011) with our SED-fitting based L_{5100} (before extinction correction), the derived correlation slope changes to -0.146 ± 0.007 ($r = -0.154$) for DR7 quasars. This is because continuum variation (while $[\text{OIII}]$ is non-variable) could yield artificial Baldwin effect, since individual quasars in brighter states (thus larger luminosity) tend to have smaller line EW , and vice versa (see Jiang

et al. 2006; Shu et al. 2012). Comparing line EW with continuum luminosity measured at epochs different from when the spectra were taken could reduce the effect of such bias. Using extinction-corrected SED-fitting based L_{5100} we further find a slope of -0.088 ± 0.010 ($r = -0.072$) for all DR7 quasars, and -0.034 ± 0.059 ($r = -0.015$) for the most luminous quasars analyzed in this work. Clearly, extinction, which could yield lower continuum luminosity and consequently larger $[\text{O III}]$ EW , also plays a significant role in the observed Baldwin effect of $[\text{O III}]$. Looking further into the Baldwin effect (and of other lines) is however beyond the scope of this work.

We then perform partial correlation to control the effects of bolometric luminosity and SMBH mass, to derive the intrinsic correlations coefficients between $\text{EW}_{[\text{OIII}]5007}$ and $\text{CF}(\lambda)$ (see Fig. 3)⁶. The partial correlation coefficients are slightly different from but similar to those of direct correlations. Below we proceed with the partial correlation results. The correlation coefficients $r(\lambda)$ derived using $\text{CF}(\lambda)$ obtained with spline fitting and linear interpolating the photometric SED are consistent within statistical uncertainties. Therefore, both approaches (spline and linear interpolation), without the need to model the SED with physical templates, could yield consistent scientific results presented below. Hereafter, unless otherwise stated, we adopt the $r(\lambda)$ resulted from linear interpolation (blue line in the lower panel of Fig. 3) for further physical interpretation.

We see clear intrinsic anti-correlations between $\text{EW}_{[\text{OIII}]5007}$ and $\text{CF}(\lambda)$ at short wavelengths. The $r(\lambda)$ reaches a minimum of -0.197 (spline) and -0.195 (linear interpolation) at rest-frame wavelength $2.1 \mu\text{m}$, corresponding to p-value of 6.3×10^{-14} and 2.7×10^{-14} for the anti-correlation. Therefore, for the first time we have detected statistically significant anti-correlation between $\text{EW}_{[\text{OIII}]5007}$ and dust emission (the simple prediction of the unification model). The $r(\lambda)$ exhibits significant dependence on λ , rising with increasing λ at $> 2.1 \mu\text{m}$. Note the correlation coefficients also rises with decreasing λ at $< 2.1 \mu\text{m}$. This is because that the significant contribution of the disc component to infrared emission at such short wavelengths could smear out the negative correlation (see Appendix for simulations). Below, while physically interpreting $r(\lambda)$, we focus only on the wavelength range of $\lambda > 2.1 \mu\text{m}$.

We stress that, though the partial correlation is derived between $[\text{O III}]$ EW and $L_{\text{IR}}(\lambda)/L_{\text{bol}}$ without priorly decomposing the various dust components, the obtained correlation $r(\lambda)$ could be used to unique probe the dust emission in luminous quasars (see §4). Note since $r(\lambda)$ was derived based on $L_{\text{IR}}(\lambda)$ obtained through interpolating the broadband photometric data points, any potential sharp spectral features in $r(\lambda)$ would have been smeared out. In the future if infrared spectra are available for a large sample of sources, we would be able to obtain $r(\lambda)$ with much better spectral resolution to reveal the potential spectral features in it.

Finally, we perform linear regression between $\text{EW}_{[\text{OIII}]5007}$ and $L_{\text{IR}}(\lambda)/L_{\text{bol}}$ ($\text{EW} \sim [L_{\text{IR}}(\lambda)/L_{\text{bol}}]^{s(\lambda)}$), and multiple parameter linear regression (to control the effects of L_{bol} and SMBH mass, $\text{EW} \sim [L_{\text{IR}}(\lambda)/L_{\text{bol}}]^{s(\lambda)} * L_{\text{bol}}^a * M_{\text{BH}}^b$). The resulted regression slope (Fig. 5) exhibits statistical significance and λ dependence the same as the Pearson correlation coefficient $r(\lambda)$ does, since two approaches (linear regression and Pearson correlation) equivalently quantify the correlation.

⁶ Since $[\text{O III}]$ EW is approximately $\sim L_{\text{OIII}}/L_{\text{bol}}$, $\text{CF}(\lambda) = L_{\text{IR}}(\lambda)/L_{\text{bol}}$, and the effect of L_{bol} has been controlled in partial correlation analyses, the partial correlation between L_{OIII} and $L_{\text{IR}}(\lambda)$ is rather similar to that between $\text{EW}_{[\text{OIII}]5007}$ and $\text{CF}(\lambda)$.

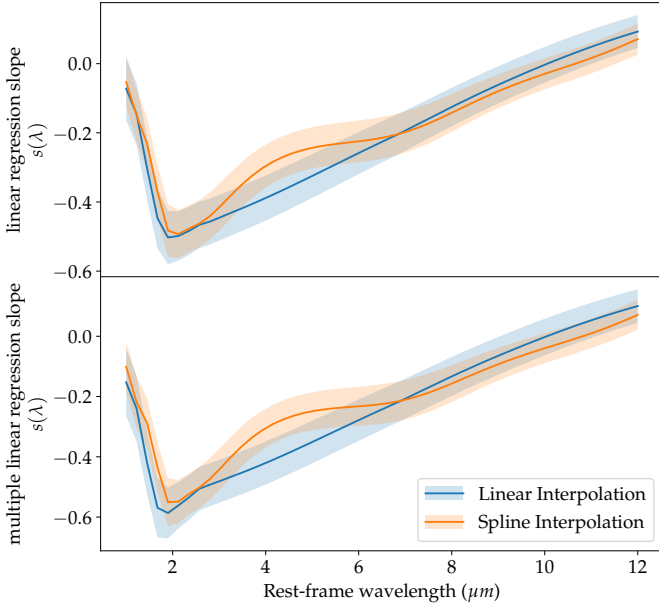


Figure 5. Similar to the middle and lower panels of Fig. 3, but here we plot the linear regression slope (upper panel), and multiple parameter linear regression slope (lower panel, controlling the effects of L_{bol} and M).

4 DISCUSSION

4.1 Simulating the $r(\lambda)$ with a physical model

To quantitatively interpret Fig. 3, we propose a model as illustrated in Fig. 6 based on the unification scheme and known knowledge in the field. The key gradients in the model include: the central SMBH, accretion disk and BLR, a equatorial torus with the innermost part differently colored as host dust, the bi-polar ionization cones resulted by the torus, and the NLR and polar dust within the ionization cones. Note in the diagram for simplicity we mark NLR clouds and polar dust clouds separately, however the NLR clouds themselves could be dusty (Netzer & Laor 1993; Mor et al. 2009; Mor & Netzer 2012), though it is yet unclear whether they dominate the polar dust emission (e.g. Alonso-Herrero et al. 2021). Another note is that the polar dust could be clumpy like the dusty NLR (e.g. Netzer & Laor 1993; Groves et al. 2006), thus its intrinsic covering factor could be significant smaller than that of the the polar cone. Nevertheless, we expect its covering factor positively correlates with that of the polar cone.

We then perform simulations to explore whether an intrinsic scatter in the solid angle of the torus (and subsequently of the ionization cone) in a sample of sources could reproduce the observed correlation between $\text{EW}_{[\text{OIII}]5007}$ and $L_{\text{IR}}(\lambda)/L_{\text{bol}}$. Below we present analyses to match the derived correlation coefficient $r(\lambda)$ (Fig. 3). Utilizing the measured regression slope $s(\lambda)$ and its uncertainty (Fig. 5) would yield consistent results.

In addition to the solid angle of the ionization cone and the equatorial torus, there are other factors which may affect the correlation between $\text{EW}_{[\text{OIII}]5007}$ and $\text{CF}(\lambda)$, and also the large scatter in themselves. First of all, the UV/optical emission from quasars are significantly variable at timescales of months to years (e.g. Ulrich et al. 1997), while [OIII] and dust emission are produced at larger scales thus are less variable. The variation of the disc component in individual quasars could lead to artificial positive correlation be-

tween $\text{EW}_{[\text{OIII}]5007}$ and $\text{CF}(\lambda)$ as both quantities anti-correlate with UV/optical continuum luminosity. Dust attenuation to UV/optical continuum are significant in some quasars. The attenuation to the continuum, which could lead to larger $\text{EW}_{[\text{OIII}]5007}$, is expected to be stronger in sources with higher solid angle of dust, thus higher $\text{CF}(\lambda)$. A similar effect is also expected if the UV SED of quasars has intrinsic scatter. For instance, a harder UV SED could yield larger $\text{EW}_{[\text{OIII}]5007}$ because of the relatively stronger ionization continuum, and meantime stronger re-processed dust emission. Such effects, if significant, would yield λ -independent positive correlation, contrary to the negative correlation discovered in this work, and shall strengthen the results of this work. Nevertheless, these factors should also be taken into account in our modeling.

4.1.1 The anti-correlation between $\text{EW}_{[\text{OIII}]5007}$ and dust emission

We first assume all dust emission comes from the equatorial torus. As the first step, we simulate a set of the ionization cone solid angle μ_i (normalized by 4π) randomly sampled from a Gaussian distribution (with a mean of 0.5 for luminous AGNs, Netzer 2015) and an undetermined standard deviation σ . We drop nonphysical values of μ_i (>1 or <0). We further produce a uniform random number between 0 and 1 for each μ_i and drop μ_i if it is smaller than the corresponding random number. This is to mimic the observational effect that type 1 quasars are more likely to be detected in systems with larger μ_i . We then model the $\text{EW}_{[\text{OIII}]5007}$ and torus CF ($L_{\text{IR}}(\lambda)/L_{\text{bol}}$) as $\text{EW}_i * A_i * \mu_i$ and $\text{CF}_i * A_i * (1 - \mu_i)$ respectively. Here A_i refers to factors which could simultaneously affect both [OIII] and torus emission per unit solid angle in individual sources, but vary from source to source. An example of such factors is flux variability in individual sources which could yield positive correlation between [OIII] EW and $L_{\text{IR}}/L_{\text{bol}}$. EW_i and CF_i represent mutually independent factors which affect the emissivity of [OIII] and dust, respectively. Note here we assume the IR emission of the torus linearly correlate with its covering factor and L_{bol} is isotropic (but see §4.2 for further discussion).

We then consider two extreme situations, and the real situation should be between the two extremes. In Case A: we drop the phase A_i , and build a set of EW_i and CF_i , both (but mutually independent) following Gaussian distributions in logarithm space with undetermined standard deviations. We then obtain $\text{EW}_i * \mu_i$ and $\text{CF}_i * (1 - \mu_i)$ to simulate the dependence of $\text{EW}_{[\text{OIII}]5007}$ and torus CF on the solid angle. We now calculate the variance and covariance of the simulated $\text{EW}_i * \mu_i$ and $\text{CF}_i * (1 - \mu_i)$, and match the three quantities to those from the real sample (at the wavelength with minimum $r(\lambda)$) to obtain the three undetermined parameters aforementioned, and then fix them for further studies. In Case B, we drop the phase CF_i assuming there in no independent factor which only impacts the dust emissivity per unit solid angle without affecting [OIII] emissivity simultaneously, and the $\text{EW}_{[\text{OIII}]5007}$ and torus CF are modeled as $\text{EW}_i * A_i * \mu_i$ and $A_i * (1 - \mu_i)$. Here the phase EW_i has to be kept, as the observed scatter in $\text{EW}_{[\text{OIII}]5007}$ (0.397 dex) is larger than that of CF_0 (0.218 dex) thus there must be additional independent factors which affect only the $\text{EW}_{[\text{OIII}]5007}$. Following the processes described for Case A, we would also derive the undetermined parameters for Case B.

To reproduce the minimum $r(\lambda) = -0.195$ we derived, in Case A, we obtain a σ_μ of 0.139, and the scatter of μ_i could account for 10% and 52% of the observed scatter in $\text{EW}_{[\text{OIII}]5007}$ and CF_0 , respectively. In Case B, a larger σ_μ (0.158) is needed to reproduce the observed anti-correlation. In Case B, σ_μ (and σ_{A_i} which is 0.087 dex) account for 13% and 82% (5% and 18%) of the observed scatter in $\text{EW}_{[\text{OIII}]5007}$ and CF_0 , respectively.

We stress that in our modeling we have modeled not only the co-

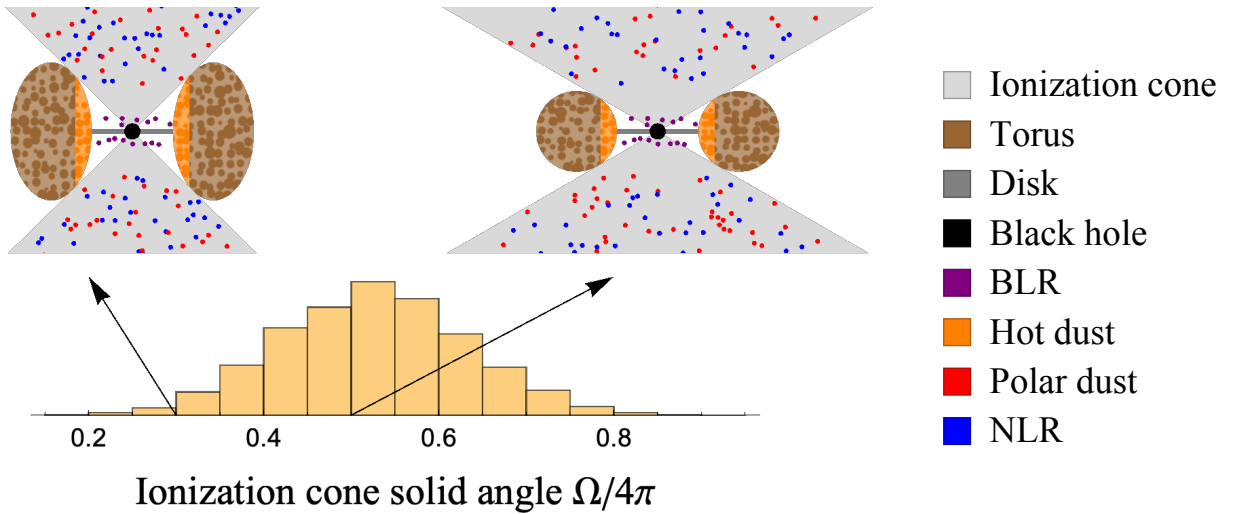


Figure 6. Illustrations of the central structures (color-labelled) of quasars with ionization cone solid angle $\Omega/4\pi = 0.3$ and 0.5 , respectively. Larger Ω would lead to stronger [OIII] 5007 line from NLR and stronger IR emission from the polar dust, both located within the ionization cone, but weaker IR emission from the torus (including hot dust). Assuming a distribution of $\Omega/4\pi$ (yellow histogram, with a mean of 0.5), we could simulate the correlation between [O III] EW and dust emission for a sample of quasars. Figures are not to scale. Note the torus/hot dust are believed to be clumpy (Krolik & Begelman 1988; Nenkova et al. 2008), and the simple illustrations here do not imply the torus has smooth boundaries.

variance between $EW_{[\text{OIII}]5007}$ and $CF(\lambda)$ but also the variance of themselves. Besides the torus's solid angle, we also have considered the effects of other factors which may affect $EW_{[\text{OIII}]5007}$ or $CF(\lambda)$ independently or affect both simultaneously, under two extreme cases (Case A and Case B). As shown previously, these additional factors may play dominant roles in producing the observed large scatter in $EW_{[\text{OIII}]5007}$. Though the variation in the torus's covering factor may only contribute a small fraction ($\sim 10\text{--}13\%$) of the observed scatter of $EW_{[\text{OIII}]5007}$, thanks to the sufficiently large sample adopted in this work, we have been able to statistically detect its effect, i.e., the anti-correlation between $EW_{[\text{OIII}]5007}$ and $CF(\lambda)$.

4.1.2 The polar dust contribution

We then simulate the contribution of the polar dust which is assumed to linearly correlate with μ_i . Now in Case A, the total simulated dust CF is $CF_i \cdot (1 - \mu_i) + f(\lambda) \cdot CF_i \cdot \mu_i$, while $EW_{[\text{OIII}]5007}$ is modeled as $EW_i \cdot \mu_i$. In case B, we model the total dust CF and $EW_{[\text{OIII}]5007}$ as $A_i \cdot (1 - \mu_i) + f(\lambda) \cdot A_i \cdot \mu_i$ and $EW_i \cdot A_i \cdot \mu_i$, respectively. The total dust CF is λ dependent, with the second part accounting for emission from the polar dust, and $f(\lambda)$ the emissivity of polar dust relative to that of torus. Since the polar dust emission positively correlates with [OIII] EW, the larger $f(\lambda)$, the weaker anti-correlation or stronger positive correlation between [OIII] EW and dust CF would be produced. Assuming there is zero polar dust contribution at wavelength with minimum $r(\lambda)$, and matching the covariance between simulated $EW_i \cdot \mu_i$ and $CF_i \cdot (1 - \mu_i) + f(\lambda) \cdot CF_i \cdot \mu_i$ with the observed $r(\lambda)$, we could solve out $f(\lambda)$ and then calculate the average fraction of polar dust contribution to total dust emission (as shown in Fig. 7). Note in Case B weaker polar dust contribution is required at given λ compared with Case A. This is because in Case A, only the term μ_i contributes to the positive correlation between [OIII] and polar dust emission, while in Case B both μ_i and A_i make the contribution.

The polar dust contribution fraction rises from 0 at $2.1 \mu\text{m}$ (as assumed) to between $\sim 39\%$ and 62% (for Case B and Case A respectively) at rest-frame $12 \mu\text{m}$, and overall contribution of the polar

dust from $1 - 12 \mu\text{m}$ is between $\sim 16\%$ – 23% . In Fig. 7 we plot the mean dust SEDs for our sample. The mean SEDs derived from various fitting/interpolating approaches are somehow different. For spline fitting and linear interpolation, we subtract the best-fit disc component obtained with the hot+cold dust model SED fitting, to derive the dust component. Note none of these mean dust SEDs is perfect, considering the hot+cold dust model fitting yielded systematical residuals (see Fig. 2), while spline and linear interpolation have smeared out physical features in the mean SED.

The mean polar dust SED could then be derived using the polar dust contribution fraction we obtained. Gray body of 1000 K , 500 K , 250 K and 100 K (with an emissivity index of 1.6 , Toba et al. 2021) are over-plotted in Fig. 7 for comparison. Clearly the mean polar dust SED we derived is considerably redder than that of the total dust emission. Fitting them approximately with a gray body yields temperature of $\sim 405\text{--}559 \text{ K}$. Unlike the fraction of polar dust contribution, the shape of the derived mean polar dust SED is less sensitive to the condition we assumed (Case A or B, see Fig. 7). These mean SEDs (available at <http://home.ustc.edu.cn/~wul/emil.html>) could be adopted in future SED fittings.

Note due to the limited wavelength range, the approximate gray body temperature we derived could be subject to significant uncertainties. Nevertheless, a redder polar dust emission is qualitatively consistent with the NLR dust models, e.g., Schweitzer et al. (2008) and Mor et al. (2009), which calculated the expected emission of NLR dust, assuming the NLR dust is concentrated in a thin spherical shell. Mor et al. (2009) obtained the mean NLR dust emission of 26 quasars through fitting their Spitzer $2\text{--}35 \mu\text{m}$ spectra with three dust components (hot dust, torus, and NLR dust). While their results could be significantly model/template dependent, it is interesting to note their best-fit NLR dust emission appears even redder, and their mean NLR dust contribution fraction rapidly drops at $< 10 \mu\text{m}$, becoming negligible at $< 8 \mu\text{m}$ (Fig. 4 of Mor et al. 2009). This suggests that either NLR is not the only location of polar dust that warmer polar dust also exists at scales smaller than NLR, or a thin spherical shell model for NLR dust is over-simplified. The fact that the mean polar

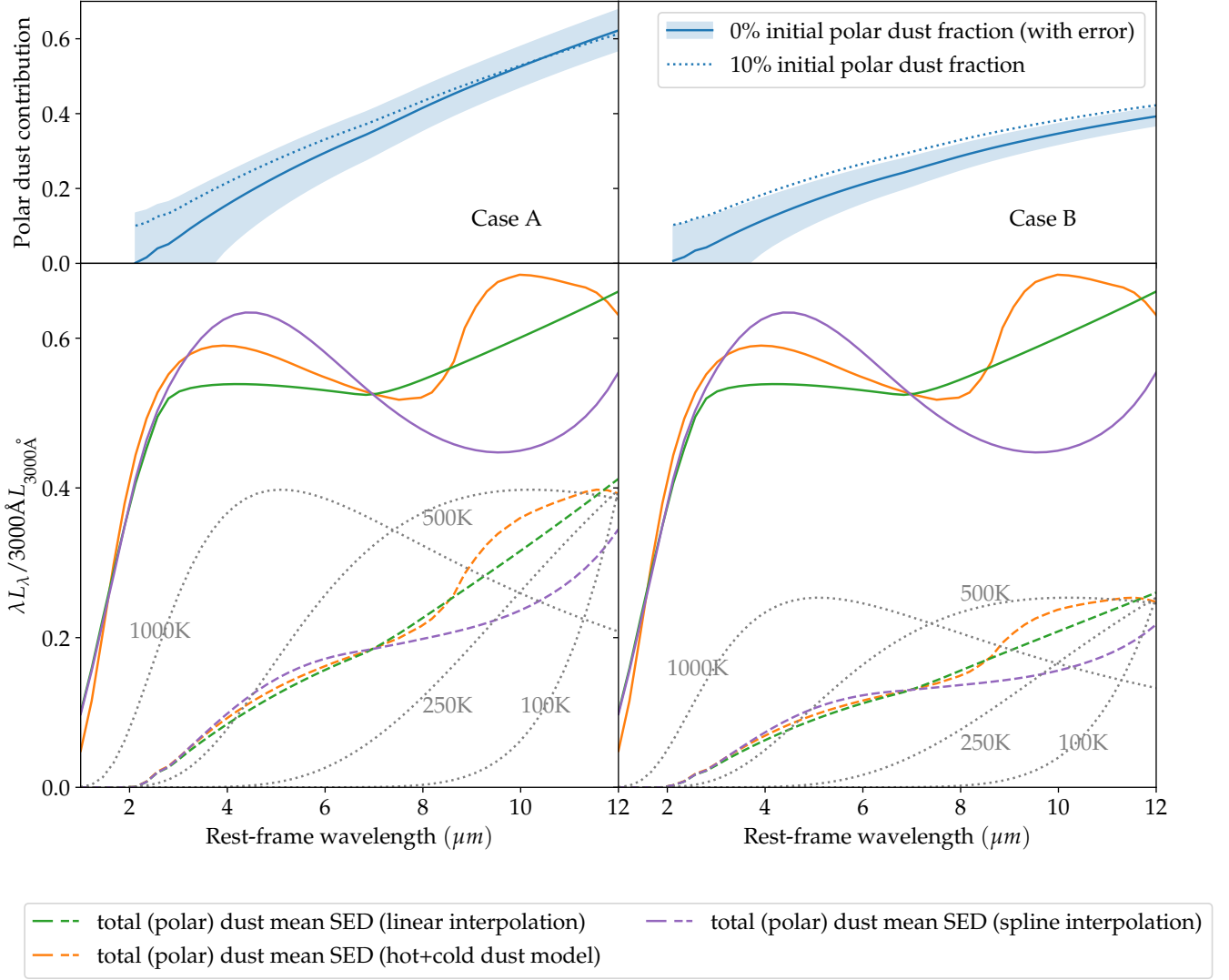


Figure 7. Upper: mean polar dust contribution fraction to total dust emission as a function of λ , converted from $r(\lambda)$ under two extreme conditions (left: Case A; right Case B. see text for definition). The blue lines are derived assuming zero polar dust contribution at $2.1 \mu\text{m}$ where the minimum $r(\lambda)$ is detected, and shadows are converted from the statistical uncertainties in $r(\lambda)$ as shown in Fig. 3. The dashed lines are derived assuming 10% polar dust contribution at $2.1 \mu\text{m}$. Lower: The mean SED of the total dust emission (solid lines) of the sample, and of the polar dust emission (dashed lines). Gray bodies with temperature of 100K, 250K, 500K and 1000K (dotted) are plotted for comparison.

dust SED we derived in Fig. 7 clearly deviates from a single temperature gray body also suggests a complicated geometry/distribution of the polar dust. Note again any potential sharp spectral features (such as the silicate emission feature at $\sim 10 \mu\text{m}$ expected from the dusty NLR, Schweitzer et al. 2008; Mor & Netzer 2012) would also have been smeared out in the mean polar dust SED. In the future applying the technique we developed in this work to a large set of infrared spectra, we would be able obtain a mean spectrum (instead of a smoothed SED) of polar dust in quasars.

We note that it is a bit arbitrary to assume zero polar dust contribution at wavelength with minimum $r(\lambda)$. Nevertheless, it has to be rather small at short wavelengths considering the observed negative correlation. In fact the mean polar dust SED derived from modeling $r(\lambda)$ is insensitive to this assumption. For instance, assuming a 10% contribution of polar dust to total dust emission at wavelength with

minimum $r(\lambda)$ barely changes the overall results (see the blue dashed line in the upper panels of Fig. 7).

Another note is that we have assumed a mean torus covering factor of 0.5 (Netzer 2015) in our modeling. In fact, assuming $L_{\text{dust}}/L_{7.8 \mu\text{m}} \sim 3$ (Weedman et al. 2012), we obtain a median $L_{\text{dust}}/L_{\text{bol}} \sim 0.314$ for our sample. Considering the extra uncertainties involved when converting $L_{\text{dust}}/L_{\text{bol}}$ to torus covering factor, including the uncertainties in bolometric luminosity, possible sample selection bias⁷ and possible anisotropy in central emission (Netzer 2015), we have adopted 0.5 instead of 0.314 in this work. Meanwhile, utilizing smaller mean torus covering factor does alter the derived mean polar dust contribution fraction (the smaller mean torus covering factor, the

⁷ Note our sample was selected to have L_{bol} (converted from L_{5100}) above 10^{46} erg/s. Sources selected to have large L_{bol} naturally tend to have smaller $L_{\text{dust}}/L_{\text{bol}}$.

larger mean polar dust contribution fraction, as expected). However the shape of the derived mean polar dust SED barely changes.

4.2 Effects of possibly anisotropic of disk radiation

In §4.1 we have assumed the dust emission (of torus and polar dust) linearly correlates with the solid angle of torus and the ionization cone, respectively. This assumption is valid if both the dust and disk emission are isotropic. While for type 1 quasars it is reasonable to assume the torus emission is isotropic (Stalevski et al. 2012; Stalevski et al. 2016), and so does the polar dust emission at larger scale, the radiation of the accretion disk might be anisotropic as proposed by Netzer (1987):

$$L(\theta) \propto \cos\theta(2\cos\theta + 1) \quad (1)$$

where θ is the angle between the line of sight and the axis of the disk. The anisotropic disk radiation would subsequently yield a nonlinear relation between $L_{\text{IR}}/L_{\text{bol}}$ and torus covering factor (see the middle panel of Figure 7 in Stalevski et al. 2016). Nevertheless, because the relation is strictly monotonic, it has little effect on the correlation coefficients we presented in §3, though it could affect the physical modeling to $r(\lambda)$ in §4.1.

The $\text{EW}_{[\text{OIII}]5007}$ could also be sensitive to the inclination angle if the disk emission is anisotropic (Risaliti et al. 2011). Bisogni et al. (2019) found type 1 quasars with larger $\text{EW}_{[\text{OIII}]5007}$ tend to have redder infrared SEDs, and attribute it to the inclination effect that the torus emission is redder at larger inclination angle. However, the inclination angle dependence of the torus emission in type 1 quasars is expected to be rather weak as the clouds are believed to be clumpy (e.g. Stalevski et al. 2012). Furthermore, in case of anisotropic disk emission, as the observed L_{UV} would be sensitive to the inclination, and both $L_{\text{IR}}(\lambda)/L_{\text{bol}}$ and $\text{EW}_{[\text{OIII}]5007}$ anti-correlate with the observed L_{UV} , the inclination effect should yield artificial positive $r(\lambda)$ between $L_{\text{IR}}(\lambda)/L_{\text{bol}}$ and $\text{EW}_{[\text{OIII}]5007}$, contrary to the clear negative correlation we discovered. If the disk emission is indeed anisotropic as shown in Equation 1, we could develop a fix to the modeling of $r(\lambda)$ given in §4.1. We previously model L_{IR} as $\text{CF}_i * A_i * (1 - \mu_i)$, and it now needs to be corrected to $\text{CF}_i * A_i * k(\mu_i)(1 - \mu_i)$, where $k(\mu_i)$ is the nonlinear correction function from torus covering factor to L_{IR} given by Stalevski et al. (2016). Compared with §4.1, a considerably larger scatter in μ_i would be then required to explain the observed negative $r(\lambda)$ at short wavelength. Furthermore, including the factor $k(\mu_i)$ would yield significantly larger scatter in L_{IR} at given scatter of μ_i (see Figure 7 in Stalevski et al. 2016). Taking these new factors into consideration, we failed to reproduce the observed $r(\lambda)$ following the procedures in §4.1, as the observed scatter of $L_{\text{IR}}/L_{\text{bol}}$ (0.218 dex for CF0) is too small to enable sufficiently large scatter in μ_i . Thus the anisotropic scenario of disk emission is disfavored. While anisotropy weaker than Equation 1 could still be feasible, we would defer further exploration on this issue to a future dedicated work.

We note the $\text{EW}_{[\text{OIII}]5007}$ dependent infrared SED slope reported by Bisogni et al. (2019) may qualitatively explained by our model that quasars with higher solid angle of the ionization cone (thus larger $\text{EW}_{[\text{OIII}]5007}$) have stronger contribution from the cooler polar dust (thus redder infrared SED). Quantitative analyses are deferred to a future work. Interestingly, a most recent study of Lyu & Rieke (2022) also found quasars with larger forbidden line EWs tend to have redder infrared colors, and they attributed this correlation to stronger polar dust contribution (which is well consistent with the scenario developed in this work).

5 SUMMARY

We analyze the correlation between $[\text{OIII}] 5007$ EW and near- to mid- infrared dust emission of a sample of luminous SDSS quasars with bolometric luminosity above 10^{46} erg/s. The ratio of infrared to bolometric luminosity $L_{\text{IR}}(\lambda)/L_{\text{bol}}$ for each quasar is measured through interpolating the photometric data from SDSS, 2MASS and WISE. The correlation efficient $r(\lambda)$ between $\text{EW}_{[\text{OIII}]5007}$ and $L_{\text{IR}}(\lambda)/L_{\text{bol}}$ for the sample is obtained as a function of infrared wavelength λ . We derive the following key findings:

1. We detect statistically robust anti-correlation between $\text{EW}_{[\text{OIII}]5007}$ and hot dust emission in luminous quasars. This directly confirms the “simple but had never been confirmed” prediction of the unification scheme of AGNs, that sources with larger solid angle of the equatorial torus (thus stronger dust emission) must have smaller solid angle of the ionization cone (thus weaker $[\text{OIII}]$ emission).

2. The anti-correlation between $\text{EW}_{[\text{OIII}]5007}$ and $L_{\text{IR}}(\lambda)/L_{\text{bol}}$ gradually weakens toward longer wavelength (at which $L_{\text{IR}}(\lambda)/L_{\text{bol}}$ is calculated) from 2 to 12 μm . This indicates there exists an extra cooler dust component, i.e., the polar dust, with its emission positively correlating with the solid angle of the ionization cone, which could reduce the anti-correlation between $\text{EW}_{[\text{OIII}]5007}$ and total dust emission at longer wavelengths.

3. Fitting the derived anti-correlation efficient $r(\lambda)$ with a physical model based on the unification scheme, we find the polar dust contribution to total dust emission gradually increases with wavelength, and reaches between 39%–62% (model dependent) at rest frame 12 μm . Multiplying the mean total dust SED of the sample and the polar dust contribution fraction we derived, we obtain a mean polar dust SED which could be used for future SED fitting.

ACKNOWLEDGEMENTS

We thank the anonymous referee for constructive comments that have significantly improved the manuscript. This work was supported by the National Science Foundation of China (No. 1890693, 12033006 & 12192221). The authors gratefully acknowledge the support of Cyrus Chun Ying Tang Foundations.

Data availability

All data used in this work comes from the Sloan Digital Sky Survey data release 7 quasar catalogue, which can be downloaded from <https://users.obs.carnegiescience.edu/yshen/BH-mass/dr7.htm>.

REFERENCES

- Alonso-Herrero A., et al., 2021, *A&A*, 652, A99
 Antonucci R., 1993, *Annual Review of Astronomy and Astrophysics*, 31, 473
 Asmus D., 2019, *Monthly Notices of the Royal Astronomical Society*, 489, 2177
 Asmus D., Hönig S. F., Gandhi P., 2016, *ApJ*, 822, 109
 Baldwin J. A., 1977, *ApJ*, 214, 679
 Baldwin J. A., Burke W. L., Gaskell C. M., Wampler E. J., 1978, *Nature*, 273, 431

- Barvainis R., 1987, *ApJ*, **320**, 537
- Bisogni S., Lusso E., Marconi A., Risaliti G., 2019, *MNRAS*, **485**, 1405
- Calderone G., Sbarrato T., Ghisellini G., 2012, *MNRAS*, **425**, L41
- Carpenter J. M., 2001, *The Astronomical Journal*, **121**, 2851
- Croom S. M., et al., 2002, *MNRAS*, **337**, 275
- Eaton M., 1983, *Multivariate Statistics: A Vector Space Approach*. Wiley, pp 116–117, <https://books.google.com.au/books?id=1CvvAAAAAAAJ>
- Eisenstein D. J., et al., 2011, *AJ*, **142**, 72
- Evans I. N., Ford H. C., Kinney A. L., Antonucci R. R. J., Armus L., Caganoff S., 1991, *ApJ*, **369**, L27
- Fukugita M., Ichikawa T., Gunn J. E., Doi M., Shimasaku K., Schneider D. P., 1996, *The Astronomical Journal*, **111**, 1748
- Gordon K. D., Clayton G. C., Misselt K. A., Landolt A. U., Wolff M. J., 2003, *The Astrophysical Journal*, **594**, 279
- Groves B., Dopita M., Sutherland R., 2006, *A&A*, **458**, 405
- Hönig S. F., Kishimoto M., 2017, *ApJ*, **838**, L20
- Jaffe W., Ford H., Ferrarese L., van den Bosch F., O’Connell R. W., 1996, *ApJ*, **460**, 214
- Jiang P., Wang J. X., Wang T. G., 2006, *ApJ*, **644**, 725
- Kellermann K. I., Sramek R., Schmidt M., Shaffer D. B., Green R., 1989, *AJ*, **98**, 1195
- Kovačević J., Popović L. Č., Dimitrijević M. S., 2010, *ApJS*, **189**, 15
- Krolik J. H., Begelman M. C., 1988, *ApJ*, **329**, 702
- Lawrence A., et al., 2007, *MNRAS*, **379**, 1599
- Leftley J. H., Tristram K. R. W., Hönig S. F., Asmus D., Kishimoto M., Gandhi P., 2021, *The Astrophysical Journal*, **912**, 96
- López-Gonzaga N., Burtscher L., Tristram K. R. W., Meisenheimer K., Schartmann M., 2016, *A&A*, **591**, A47
- Lyke B. W., et al., 2020, *ApJS*, **250**, 8
- Lyu J., Rieke G. H., 2022, arXiv e-prints, p. arXiv:2210.08037
- Ma X.-C., Wang T.-G., 2013, *Monthly Notices of the Royal Astronomical Society*, **430**, 3445
- Maiolino R., Shemmer O., Imanishi M., Netzer H., Oliva E., Lutz D., Sturm E., 2007, *A&A*, **468**, 979
- Mor R., Netzer H., 2012, *MNRAS*, **420**, 526
- Mor R., Trakhtenbrot B., 2011, *ApJ*, **737**, L36
- Mor R., Netzer H., Elitzur M., 2009, *ApJ*, **705**, 298
- Müller-Sánchez F., Prieto M. A., Hicks E. K. S., Vives-Arias H., Davies R. I., Malkan M., Tacconi L. J., Genzel R., 2011, *ApJ*, **739**, 69
- Neškova M., Sirocky M. M., Nikutta R., Ivezić Ž., Elitzur M., 2008, *ApJ*, **685**, 160
- Netzer H., 1987, *MNRAS*, **225**, 55
- Netzer H., 2015, *Annual Review of Astronomy and Astrophysics*, **53**, 365
- Netzer H., Laor A., 1993, *ApJ*, **404**, L51
- Netzer H., Shemmer O., Maiolino R., Oliva E., Croom S., Corbett E., di Fabrizio L., 2004, *ApJ*, **614**, 558
- Nikutta R., Lopez-Rodriguez E., Ichikawa K., Levenson N. A., Packham C., Hönig S. F., Alonso-Herrero A., 2021, *ApJ*, **919**, 136
- Risaliti G., Salvati M., Marconi A., 2011, *MNRAS*, **411**, 2223
- Roseboom I. G., Lawrence A., Elvis M., Petty S., Shen Y., Hao H., 2013, *Monthly Notices of the Royal Astronomical Society*, **429**, 1494
- Schneider D. P., et al., 2010, *The Astrophysical Journal*, **139**, 2360
- Schweitzer M., et al., 2008, *ApJ*, **679**, 101
- Shang Z., et al., 2011, *ApJS*, **196**, 2
- Shen Y., et al., 2011, *The Astrophysical Journal Supplement Series*, **194**, 45
- Shu X. W., Wang J. X., Yaqoob T., Jiang P., Zhou Y. Y., 2012, *ApJ*, **744**, L21
- Stalewski M., Fritz J., Baes M., Nakos T., Popovic L. C., 2012, *Publications de l’Observatoire Astronomique de Beograd*, **91**, 235
- Stalewski M., Ricci C., Ueda Y., Lira P., Fritz J., Baes M., 2016, *Monthly Notices of the Royal Astronomical Society*, **458**, 2288
- Stalewski M., Tristram K. R. W., Asmus D., 2019, *MNRAS*, **484**, 3334
- Storchi-Bergmann T., et al., 2018, *ApJ*, **868**, 14
- Toba Y., et al., 2021, *The Astrophysical Journal*, **912**, 91
- Ulrich M.-H., Maraschi L., Urry C. M., 1997, *ARA&A*, **35**, 445
- Urry C. M., Padovani P., 1995, *PASP*, **107**, 803
- Wang H., Xing F., Zhang K., Wang T., Zhou H., Zhang S., 2013, *ApJ*, **776**, L15
- Weedman D., Sargsyan L., Lebouteiller V., Houck J., Barry D., 2012, *ApJ*, **761**, 184
- Whittaker J., 2009, *Graphical Models in Applied Multivariate Statistics*. Wiley Publishing
- Wright E. L., et al., 2010, *The Astronomical Journal*, **140**, 1868
- Yang G., et al., 2020, *MNRAS*, **491**, 740
- Zhang K., Dong X.-B., Wang T.-G., Gaskell C. M., 2011, *ApJ*, **737**, 71
- Zhang K., Wang T.-G., Gaskell C. M., Dong X.-B., 2013, *ApJ*, **762**, 51

APPENDIX A: THE RELIABILITY OF THE $R(\lambda)$

The derived correlation coefficients between $CF(\lambda)$ and $EW_{[\text{OIII}]5007}$ show sharp rise toward shorter wavelength at $< 2 \mu\text{m}$ (see Fig. 3). This is simply because that the significant contribution of the disc component to near infrared could smear out the negative correlation. Below we present simulations to verify.

We first construct a mock sample of artificial CF0 and $EW_{[\text{OIII}]5007}$ with their statistical properties consistent with those of the real quasar sample but with a wavelength-independent intrinsic correlation coefficient between $CF(\lambda)$ and $EW_{[\text{OIII}]5007}$. To do so, we first calculate mean vector and covariance matrix of the four variables: CF0, EW, L_{bol} and M_{BH} .

$$\mu = \begin{bmatrix} \mu_1 \\ \mu_2 \end{bmatrix} \text{ with sizes } \begin{bmatrix} 2 \times 1 \\ 2 \times 1 \end{bmatrix}$$

$$\Sigma = \begin{bmatrix} \Sigma_{11} & \Sigma_{12} \\ \Sigma_{21} & \Sigma_{22} \end{bmatrix} \text{ with sizes } \begin{bmatrix} 2 \times 2 & 2 \times 2 \\ 2 \times 2 & 2 \times 2 \end{bmatrix}$$

where subscript 1 corresponds to CF0 and EW and subscript 2 corresponds to L_{bol} and M_{BH} .

Inversion of a covariance matrix yields partial correlation matrix and vice versa (Whittaker 2009). So we can modify the matrix element corresponding to CF0 and EW in the yielded partial correlation matrix and obtain covariance matrix with appointed partial correlation coefficient between CF0 and EW and keep correlations between other variables unchanged. Using this new covariance matrix Σ , we construct a 4-dimensional log-normal distribution $N(\mu, \Sigma)$. For a given source in the sample, L_{bol} and M_{BH} are given by observations (denoted as \mathbf{a}), its simulated CF0 and EW are sampled from the conditional distribution $N(\bar{\mu}, \bar{\Sigma})$, where $\bar{\mu} = \mu_1 + \Sigma_{12}\Sigma_{22}^{-1}(\mathbf{a} - \mu_2)$, $\bar{\Sigma} = \Sigma_{11} - \Sigma_{12}\Sigma_{22}^{-1}\Sigma_{21}$ (Eaton 1983). The simulated CF0 and EW are thus guaranteed to have distributions (mean and scatter) consistent with those of the real sample (CF0 from the hot+cold dust model fitting, and EW from SDSS spectra), but with assigned intrinsic correlation between them.

We could then build mock SED data points for each source with the simulated CF0 and EW. We adjust the normalization of the mean dust component (see Fig. 7) to match the simulated CF0 for each source, and add the dust component to the best-fit disk component derived from the hot+cold dust model fitting. Convolving the mock SED model with the transmission curves of photometric bands, and adding the residuals obtained through fitting the real SED (see Fig. 1), we build mock SED data points for each source.

Repeating the SED interpolation and correlation analyses, we could derive $r(\lambda)$ for the mock sample. For various input correlation coefficients, the output $r(\lambda)$ derived from the mock samples quickly converge to zero at $\lambda < 2 \mu\text{m}$. Comparing the $r(\lambda)$ of the real and mock sample, we can claim that the rise of the observed $r(\lambda)$ with decreasing wavelength at λ smaller than $\sim 2.1 \mu\text{m}$ is clearly an artifact. This is because at such short wavelengths, the contribution

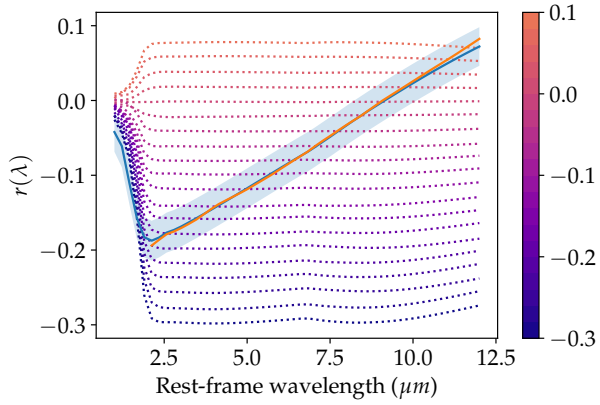


Figure A1. Monte-Carlo simulations show how the mock wavelength-independent correlation coefficients (with 20 input values varying from -0.3 to 0.08, with a step size of 0.02) could be recovered (color coded dotted lines) in mock samples. The blue line plots the $r(\lambda)$ derived from the real sample, while the the yellow line shows the corrected $r(\lambda)$ after registering with the simulated $r(\lambda)$. Clearly, such correction is negligible (compared with the statistical uncertainties which are plotted as blue shadows) at $\lambda > 2.1 \mu\text{m}$, while at shorter wavelengths reliable correction would be infeasible.

to total photometry from the disc component could outshine the dust component (see Fig. 1), which could subsequently smear out the anti-correlation between $\text{CF}(\lambda)$ and EW. The $r(\lambda)$ from the mock samples appear flat (though subtle curvatures are visible) at $\lambda > 2.1 \mu\text{m}$, and the input wavelength-independent correlation coefficients r can be well recovered. The subtle curvatures at $\lambda > 2.1 \mu\text{m}$ are due to weak biases in our SED analyses (interpolation could yield extra scatter) and the wavelength-dependent photometric uncertainties (see Fig. 2). However such biases are negligible in this work.

This paper has been typeset from a $\text{T}_{\text{E}}\text{X}/\text{L}^{\text{A}}\text{T}_{\text{E}}\text{X}$ file prepared by the author.